Journal Name

ARTICLE TYPE

Cite this: DOI: 00.0000/xxxxxxxxxx

Titanium and titanium oxides at the K- and L-edges: comparing theoretical calculations to X-ray absorption and X-ray emission measurements†

Karina Bzheumikhova,[a‡] John Vinson,[b] Rainer Unterumsberger, [a,c] Malte Wansleben, [a,c] Claudia Zech, [a] Kai Schüler, [a] Yves Kayser, [a] Philipp Hönicke, [a], Burkhard Beckhoff, [a]

Received Date
Accepted Date

DOI: 00.0000/xxxxxxxxxx

Using well-calibrated experimental data we demonstrate the applicability of theoretical X-ray absorption spectroscopy (XAS) as well as X-ray emission spectroscopy (XES) calculations for titanium (Ti), titanium oxide (TiO), and titanium dioxide (TiO_2) at the Ti K and L edges as well as O K edge. XAS and XES in combination with a multi-edge approach offer a detailed insight into the electronic structure of materials since both the occupied and unoccupied states are probed. The experimental results are compared with *ab initio* calculations from the OCEAN package which uses the Bethe-Salpeter equation (BSE) approach. Using the same set of input parameters for each system for calculations at different edges, the transferability of the OCEAN calculations across different spectroscopy methods and energy ranges is demonstrated. Thus, the broad applicability for analyzing and interpreting the electronic structure of materials with the OCEAN package is shown. While the results showed that the OCEAN package is a useful tool for analyzing and interpreting the electronic structure of materials, it also highlighted some discrepancies between the experimental data and the theoretical calculations, indicating some limitations of the approach.

1 Introduction

In the present study, we use titanium and several of its oxides as model systems for early 3d transition metals and employ X-ray absorption spectroscopy (XAS) and X-ray emission spectroscopy (XES) at different energy ranges (the Ti and O K edges and the Ti $L_{II,III}$ edges) to demonstrate the applicability of *ab initio* calculations using the OCEAN code[1–3]. The study of early 3d transition metal systems by means of XAS and XES provides information on the electronic structure which has an influence on material properties like charge transport and optical properties relevant in many fields including nanotechnologies and energy storage materials[4–7].

The electronic structure of these titanium systems has been previously well studied[8–12]. That is why titanium and its oxides are excellent candidates to test and validate theoretical calculation methodologies. Therefore, we use this knowledge combined with physically traceable measurement techniques with complementary discrimination and sensitivity capabilities to provide reliable validation of *ab initio* calculations based on the Bethe-Salpeter equation (BSE) approach. We show that moderately complex structures such as early transition metals like titanium can be well described using the BSE approach. The same set of OCEAN input parameters for each system is used for the calculations, which are then compared to XAS and XES data from both the K- and L-edges. The predictive power of the OCEAN code, which explicitly treats the interactions between the photo-electron and core-hole using the BSE approach, has been shown for specific cases in the past[13–16]. Wansleben, et al., provides another example of a successful comparison between OCEAN calculations with experimental XES and XAS data for iron-sulfur compounds[17]. This present work continues these investigations by demonstrating the code for a multi-edge analysis of an early transition metal.

X-ray spectroscopy techniques at different edges and energies can be used to probe distinct electron transitions and thus different parts of the electronic structure. On the other hand, the discrimination capability and sensitivity of XAS and XES at different edges vary significantly[18–20]. Quite often available instrumentation or experimental boundary conditions regarding the sample and its environment influence the type of measurement which can be conducted. In this context, a prior consideration based on calculations that need to be validated, using studies as presented in this work, will be useful to evaluate the discrimination capa-

[a] *Physikalisch-Technische Bundesanstalt, Abbestraße 2-12, 10587 Berlin, Germany*
‡ *karina.bzheumikhova@ptb.de*
[b] *Material Measurement Laboratory, National Institute of Standards and Technology, Gaithersburg, MD 20899*
[c] *Helmut Fischer GmbH Institut für Elektronik und Messtechnik, Industriestrasse 21, 71069, Sindelfingen, Germany*
† Electronic Supplementary Information (ESI) available: [details of any supplementary information available should be included here]. See DOI: 00.0000/00000000.

bility which can be expected during the experiment. It is shown that this type of consideration can be realized for different energy ranges and spectroscopic techniques. XAS probes the unoccupied part of the electronic structure of the system. The oxidation state of an element can be determined with XAS at the K edge by analyzing the edge position and the pre-edge, which can be difficult to measure and interpret. Indeed, the pre-edge of a transition metal displays the dipole-forbidden but quadrupole-allowed 1s to 3d transitions[9,21]. While dipole-forbidden transitions can be observed in weak quadrupole and mixed transitions in the pre-edge, the involved states can be observed in dipole-allowed transitions at the L edge. XES, on the other hand, probes the occupied part of the electronic structure. Specifically, the Kβ spectroscopy is of interest since the Kβ satellites K$\beta_{2,5}$ and Kβ'' are sensitive to ligand bonds of transition metals[22–24]. These are, however, challenging to measure due to the low intensity of around 2% relative to the K$\beta_{1,3}$[25], whose high-energy tail is overlapping with the satellites. We successfully complete this analysis of the ligand bonds by including oxygen K-edge experiments, which probe the core-level transitions of the oxygen atom.

A careful comparison of theoretical and experimental data requires an understanding of different factors that might have influenced the data. In order to move towards reliable and quantitative investigations, we use calibrated and well-characterized instrumentation which allows us to differentiate between instrumental, experimental, and physical contributions. For comparing experimental spectra to calculations of the electronic structure it is important that the spectra are free from instrumental and experimental contributions. These influences can partially be mitigated. Instrumental resolutions, efficiencies, and uncertainties can be optimized[26–28] and energy scales can be calibrated, optimally in a traceable manner such that a transfer to and intercomparability of different experiments with regard to the instrumentation used can be realized. To start with, this is done for our measurements by using instrumentation that has been calibrated in terms of its energy scale in a physically traceable manner and response function at selected incident and emission photon energies. The calibration of the energy scales of monochromatized synchrotron radiation allows using a common energy scale for XAS and XES measurements involving the creation of an electron vacancy in the same shell, which is necessarily collected with different instrumentation under the premise that the spectrometer used for the XES experiments can be calibrated using elastically scattered radiation. This aspect is crucial for the comparability and validation of the different calculations for XAS and XES.

2 Experimental setup and measurement procedure

All experiments were conducted in the Physikalisch-Technische Bundesanstalt (PTB) laboratory at the electron storage ring BESSY II[29,30]. XAS measurements around the K-edge were realized at the four-crystal-monochromator (FCM) beamline[31,32], while measurements around the L-edges were realized at the plane-grating monochromator (PGM) beamline[33] for undulator radiation. The beamlines provide tunable radiation in the X-ray photon energy ranges between 1.75 keV and 10 keV and 78 eV and 1860 eV, respectively, with high spectral purity and photon flux. The energy scale of the FCM beamline has been calibrated using back-reflection of single-crystals[31,32]. The energy resolution is ≈ 0.5 eV around the titanium K edge and the uncertainty is around 1.0 eV. The PGM beamline is calibrated from the absorption of well-known vibrational resonances of noble gases. The resolution of the PGM beamline around the titanium L edge is ≈ 0.23 eV and the uncertainty is around 0.5 eV[33].

The measurements shown in this work are complemented by XES K-edge measurements and calculations first published by Wansleben *et al.*[34] as well as XES and XAS measurements at the Ti L-edge published by Unterumsberger *et al.*[35]. Together they form a complete picture of the near-edge x-ray emission and absorption which we use to assess the validity of the OCEAN code across various core levels.

X-ray absorption measurements were conducted by both detecting the induced fluorescence radiation with a silicon drift detector (SDD)[36,37] as well as transmission measurements[35]. A photodiode is used to determine the incident photon energy-dependent variations in the photon flux. The samples were inserted in an ultra-high vacuum environment at an incident and takeoff angle of $\theta = 45^\circ$[26]. The instrumental influence by means of the response functions is quantified such that the different contributions in the measured spectra can be accurately discriminated. The diodes used for transmission measurements as well as the response function of the SDD used for the fluorescence radiation measurements are calibrated.

XES experiments around the Ti K edge were conducted at the dipole white light (DWL) radiation beamline[38] with a polychromatic excitation spectrum originating from a 1.3 T bending magnet. To reduce background radiation caused by scattering the polychromatic excitation spectrum was attenuated by a 2-μm-thick aluminum filter[34]. The measurements were conducted using a von Hamos spectrometer[39] based on two full-cylinder Bragg crystals, each consisting of 40-μm-thick highly annealed pyrolytic graphite (HAPG) mosaic crystals. The use of two crystals instead of one increases the resolving power of the spectrometer[40]. Further details on the instrumentation and measurement details of the titanium XES measurements around the K edge can be found in the work of Wansleben *et al.*[34].

The XES spectra around the L edges as well as the oxygen K edge were collected at the PGM beamline using a wavelength-dispersive spectrometer (WDS)[28,41,42] based on the Rowland circle geometry. The optical source, defined by means of an entrance slit, the reflective grating, and the detecting charge-coupled device (CCD) detector are all positioned on the Rowland circle which is defined by the grating curvature. A vertical slit placed between the entrance slit and the grating collimates horizontally so that the detector is not illuminated outside of its active area in the non-dispersive direction. Additionally, a horizontal slit is restricting the illuminated area of the grating in the dispersive direction defining the solid angle of acceptance of the WDS.

For the presentation of the broad applicability of the OCEAN code a set of samples was used that is well known and has been studied with X-ray spectrometry techniques[35]. Three different samples were used: Ti, TiO, and TiO_2. The used samples are titanium oxides on a thin silicon nitride window which is placed on

	Ti	TiO	TiO_2
plane-wave cutoff / Ry.	200	150	150
k-mesh	12×12×10	8×8×8	12×12×8
number of conduction bands	400	400	500
number of screening bands	700	397	1235

Table 1 OCEAN calculation convergence parameters. The plane-wave cutoff (given in Rydberg) and the conduction band number are used for the DFT calculation, whereas the k-mesh and screening band numbers are used for the BSE calculation.

a silicon wafer. Different titanium oxidation states were achieved by varying the amount of oxygen using ion beam sputter deposition (IBSD), measured in standard cubic centimeters per minute. The oxidation state of the samples depends on the oxygen flow rate. This type of thin samples is useful for transmission measurements in addition to measurements with an SDD and reduced self-absorption in the material.

3 Theoretical Modeling

The XES and XAS calculations have been carried out throughout this work using the OCEAN code[1,3]. The first-principle code OCEAN calculates core edge spectroscopy including XAS, XES, RIXS, and non-resonant X-ray scattering (NRIXS). OCEAN input includes parameters on the atomic structure, photon excitation information, pseudopotentials generated using the ONCVPSP code[43] for the density functional theory (DFT) calculation, and specific convergence thresholds for the calculations. For each system, no input parameters are changed when switching between edges or absorption and emission. Thus, the comparison of calculated results with experimental results from different energy ranges (different edges) and different types of measurements (XAS, XES) allows for a broad illustration of the code.

The general issue with 3d transition metals is the partially filled 3d-sub-shell. Early transition metals have mostly unoccupied 3d-bands, which is well described within DFT, whereas for later transition metals local or semi-local density functionals fail to sufficiently localize 3d- or 4f-electrons and underestimate the strength of the Coulomb repulsion between electrons of opposite spin in the same orbital.

Norm-conserving pseudopotentials and the local-density approximation to the exchange-correlation functional were chosen in this work. The atomic structures were taken from the Crystallography Open Database (Ti[44], TiO[45], TiO_2[46]). The plane-wave cutoff is used for the DFT calculation to truncate the basis and has been chosen as stated in Table 1. The **k**-mesh grid of the crystal momentum for the BSE was chosen to be sufficiently high within a reasonable computation time. The number of conduction and screening bands is chosen to be sufficiently high so that the number of wave functions included up to some energy above the Fermi level is well represented. Sufficiently high numbers of conduction and screening bands were achieved by increasing the respective parameter until the difference in the energy scale of the system was less than 0.01 eV. The final set of parameters is shown in Tab. 1.

4 Results and Discussion

In the following, we present the accumulated results for the XAS and XES measurements around the K and L edges for the three titanium systems Ti, TiO, and TiO_2. It is important to note, that the presented calculations are done in terms of band structure calculations on crystal structures of solids. However, for simplicity and a convenient comparison with theoretical data, the molecular-orbital (MO) model has been chosen to describe the features in the spectra[47,48]. In the MO representation titanium and oxygen build molecular orbitals which include valence electrons of titanium $4s$ and $3d$, and oxygen $2p$ as well as stronger bound $2s$ oxygen electrons and the unoccupied titanium $3d$ state. TiO and TiO_2 differ mostly in the resulting t_{2g} state. While TiO has two electrons in this state, TiO_2 has an unoccupied t_{2g} state.

As mentioned above, our samples were thin films grown on silicon nitride to facilitate transmission measurements and avoid self-absorption effects. In the case of TiO_2, there are three well-known phases at atmospheric pressure: rutile, anatase, and brookite. Brookite is unlikely in the case of oxygen flow samples due to its metastable crystal structure. Based on Ti K- and L-edge calculations of rutile and anatase as well as qualitative comparisons to literature spectra[10,49–53] the TiO_2 sample was found to be likely amorphous, as the experimental spectra differ from both rutile and anatase. This complicates our analysis because OCEAN calculations require a known, periodic structure.

The measured NEXAFS of the TiO_2 sample at the Ti K edge resembled the reference spectra for amorphous samples in literature[49–51]. Anatase or a possible linear combination of rutile and anatase was discarded due to the pre-edge region[10] and edge rise of the experimental data which resembles the rutile reference. The experimental spectrum was broad and less distinct, making a quantitative and reliable conclusion difficult. However, due to the above-mentioned reasons, and the fact that the OCEAN calculated rutile spectrum provided a good model for fitting the experimental data, the analysis at the K edge in this paper uses the rutile calculations.

The comparison of the experimental XAS L spectrum of the TiO_2 sample with the calculated spectra of rutile and anatase as well as literature spectra[52,53] confirmed the TiO_2 most likely being amorphous. However, in contrast to the K edge, the e_g related peak at the L_3 edge more closely resembles the anatase phase in terms of symmetry, thus for the L-edge analysis of TiO_2 the anatase calculations were used.

4.1 Spectral Comparison and Fitting Methodology

When comparing experimental and calculated spectra the focus lies on peak positions and shapes. The deviations in peak shape between the two are the result of both experimental and theoretical factors. One of the experimental aspects is the resolution of the instrumentation. In all the presented experimental data the resolution of the beamline and the chosen spectrometers is known. Thus, it was applied to the calculated data as an energy-independent broadening, which is sufficient in the given relatively small energy ranges for each individual experiment. The summarized broadening resulting from the instrumentation can be

found in Table 2[28,32–34]. Additionally, a theoretical broadening due to the core-hole lifetime was applied to the calculated spectra. For the titanium K edge, this is 0.94 eV, for the L edge 0.24 eV (L_{II} edge value), and for the oxygen K edge 0.13 eV[54]. It is important to note that additional broadening effects like super-Coster-Kronig decay processes and the radiative Auger effect as well as vibrational disorder are neglected in this first-order treatment[55,56].

The experimental data have an uncertainty from the respective beamline and spectrometer energy scales' uncertainties. For the measured spectra this arises due to the energy scale of the used beamlines and spectrometers. The FCM beamline energy is calibrated using a back-reflection of single crystals[32] while the PGM beamline is calibrated using resonances of noble gases[33]. This way a transferability of the energy scale is provided between different measurements. In addition, the emission energy scale for the XES measurements is defined using the elastic scattering of a material and thus transferred from the energy scale of the beamline. The energy scale of the XES K measurements is calibrated using previous measurements at the FCM beamline. There, using the monochromatic energy available the energy scale has been calibrated using the elastic scattering and then transferred to the DWL beamline. Based on continuous calibrations of the beamlines throughout the years, we determined an uncertainty of the two beamlines. For the PGM beamline, the uncertainty of the energy scale is around 0.5 eV, whereas, for the FCM beamline, it is around 1 eV.

OCEAN does not calculate an absolute energy scale. Therefore, one of the calculations is used to align the energy scale with the experimental energy scale by determining either a significant feature position or the edge position and using this offset for all other calculated data. This is done once for the Ti K edge, the Ti L edge, and the O K edge. Meaning that the energy alignment is done only once for each edge and used throughout the respective XAS and XES spectra for all three systems. In this way, the relative positions calculated with OCEAN remain intact and can be validated against the calibrated experimental data.

For further analysis of the comparison of spectra regarding the peak positions between experimental data and theoretical calculations as well as the extraction of the pre-edge peaks, a fit of all spectra was performed using Voigt profiles for the resonances and additional step functions for the step edges in the case of XAS[57,58]. A Voigt profile is described as the convolution of a Lorentzian function and a Gaussian function. The fitting was done using the Levenberg-Marquardt minimization algorithm with the LMFIT (Non-Linear Least-Square Minimization and Curve-Fitting) Python package[59,60]. The OCEAN calculations were fitted first, and then applied as a starting set of parameters to the experimental data, while certain parameters were changed to account for experimental aspects. For the experimental data fits, the residual to be minimized was calculated as a weighted residual using the statistical error of the measurements $y/\sqrt{(N)}$ (N - detected events).

The initial guess for the peak energy positions of the OCEAN calculation fit was done visually since the peaks were clearly pronounced in the spectra. The assumption that the physical amount of peaks in the experimental spectrum and calculated spectrum should be identical was made. This was shown previously in several studies of the OCEAN code[2,13,17,34,61]. Once the OCEAN fit was done, the peak positions were scaled using the energy scaling as described previously, to match the experimental energy scale. Since a slight discrepancy in relative peak positions is expected between OCEAN and experimental spectra, the boundaries for the experimental data fit were set around ± 0.8 eV in most cases.

The widths of the peaks are influenced by several factors, including the core-hole lifetime and instrumental broadening. The only ad-hoc broadening included in the OCEAN calculation is the user-provided constant approximated core-hole lifetime which is used as a constant across the whole energy scale. For the Ti-K edge this was set to 0.94 eV and for the Ti L-edges it was set to 0.24 eV[54]. In a simplified single atom (or molecule) model, one would expect the spectral features to be well fitted with a Lorentzian with the width of the lifetime broadening, and later in the experimental data an additional Gaussian with the instrumental broadening. However, it is important to note that although we are conducting calculations on a unit cell, the results of the calculations are done in terms of the band structure in a condensed phase, i.e., treating the system as a crystalline solid. This means that the shape of the spectral features is more complex and reflects the density of states, which can have a somewhat arbitrary shape. Furthermore, the measurements of the systems were done without the preference for any crystal direction. Thus, the OCEAN calculation results were averaged over orthogonal photon polarizations (momentum transfer) directions. To account for this complexity, OCEAN spectra were fitted using Voigt profiles, where the minimum boundaries for the Lorentzian were set to the user provided approximated core-hole lifetime.

The width of the peaks in the experimental spectra is influenced by several factors including the energy-dependant core-hole lifetime, the instrumental broadening, and vibration disorder. The core-hole lifetime was described by an empirical energy-dependent Lorentzian function $\gamma(E) = f_L + \alpha(E - E_0)$ with the core-hole lifetime f_L the Fermi level E_0, and a parameter α, which was allowed to vary based on literature value ranges from 0.07 eV^{-1} to 0.15 eV^{-1} for the Ti K edge[62]. The lower range of the instrumental broadening was set to values as described in Tab. 2. The step edge was described as an $\arctan()$ function for the influence of the lifetime broadening and an $\mathrm{erf}()$ function for the instrumental broadening.

The result of the minimizer was the final parameters with the confidence interval being calculated as an estimation of the standard errors from the estimated covariance matrix. For the OCEAN calculations as well as the experimental XES spectra the resulting uncertainties were good and can be used to provide an estimate of the uncertainties. For more complex experimental data with more peaks, the algorithm failed to estimate sensible uncertainties. Thus, further analysis of the result using bootstrap sampling was done. Given the original data set of size N, a bootstrap sample was generated by randomly sampling N data points with replacement from the original data. By generating multiple bootstrap samples and estimating the parameter for each sample, the bootstrap method provides an empirical distribution of the

parameter, allowing estimation of its uncertainty.

An example of a fit is shown in Fig. 1. The peaks in the fit of the calculation and the experimental spectra have a good agreement. The main differences are in relative intensity and width, which can be explained through experimental effects (vibrational disorder, secondary excitation, self-absorption) and instrumental broadening (resolution of the instrumentation). The differences in positioning are ≤ 1.1 eV.

The summary of all the peak position deviations between calculation and experimental data can be found in Tab. 3, which is explained in detail in the following sections regarding the different measurements. Deviations in the peak number are mostly due to broadening in the experiment, which precludes resolving all the features present in the calculated spectra.

Instrumentation	Res. power $E/\Delta E$	Resolution (eV)	Edge
FCM beamline	11800	0.38	Ti K
PGM beamline	2000	0.23	Ti L & O K
von Hamos	2700	1.8	Ti K
WDS (Rowl. circ.)	1100	0.4	Ti L & O K

Table 2 Summarized resolving power and resolutions from the beamlines and the spectrometers used[28,32,34]. The overall broadening resulting from each measurement was applied to the calculated data as a Gaussian broadening.

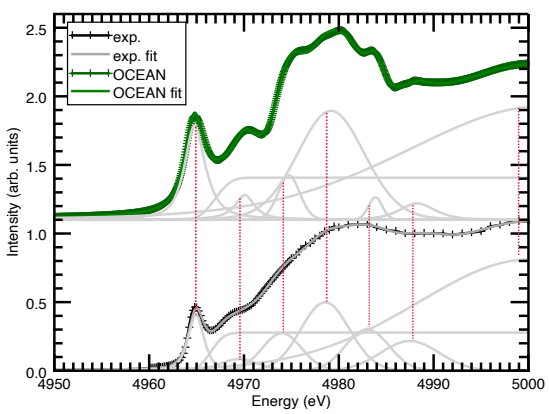

Fig. 1 Fit of K-edge XAS results of Ti as measured (bottom) and calculated with OCEAN (top). For fitting of the edge, an error function was used whereas for the peaks a pseudo-Voigt profile consisting of a linear combination of a Gaussian and a Lorentzian was used.

4.2 Titanium K-edge XAS

The obtained XAS results at the K-edge are shown in Fig. 2 as the normalized intensity as a function of the monochromatic incident photon energy. The spectra are presented normalized to the maximum intensity and offset vertically for clarity. XAS probes the transition into the unoccupied states, which results in the characteristic K-edge features A_1 and A_2. The pre-edge feature A_1 can be assigned to the $1s \rightarrow t_{2g}$ and $1s \rightarrow e_g$ quadrupole transitions[63] while the feature A_2 are the $1s \rightarrow t_{1u}$ and $1s \rightarrow t_{1u}$ transitions. Differences in the three systems can be analyzed through the shape and energy shift differences between these features. With a higher oxidation state the overall spectra shift to higher

Edge	Peak	Transition	Ti ΔE/eV	TiO ΔE/eV	TiO_2 ΔE/eV
Ti XAS-K	A_1	$1s \rightarrow 2t_{2g}, 3e_g$	0.3	-1.0	-0.1
	A_2	$1s \rightarrow 4t_{1u}, 5t_{1u}$	-1.5	- 1.0	0.2
Ti XAS-L	B_1	$2p_{3/2} \rightarrow 2t_{2g}, 3e_g$	0.2	1.2	1.9
	B_2	$2p_{1/2} \rightarrow 2t_{2g}, 3e_g$	0.4	0.6	1.6
Ti XES-K	C_1	O2s Ti3$d \rightarrow 1s$	-	-3.4	-3.8
	C_2	O2p Ti3$d \rightarrow 1s$	-1.6	-1.9	-2.7
Ti XES-L	D_1	$2e_g \rightarrow 2p_{3/2}$	-	-0.9	-
	D_2	$2t_{2g} \rightarrow 2p_{3/2}$	-0.5	-1.0	-0.1
	D_3	$2t_{2g} \rightarrow 2p_{1/2}$	-0.4	-0.5	-0.9
O XAS-K	E_1	$1s \rightarrow 2t_{2g}$	-	0.4	-0.9
	E_2	$1s \rightarrow 3e_g$	-	0.2	0.1
O XES-K	F_1	$2t_{1u} \rightarrow 1s$	-	-	-0.7
	F_2	$2_{tu}, 3t_{1u} \rightarrow 1s$	-	-0.1	-0.3
	F_3	$2t_{2g} \rightarrow 1s$	-	0.4	-

Table 3 Summarized differences between calculated and measured peak positions.

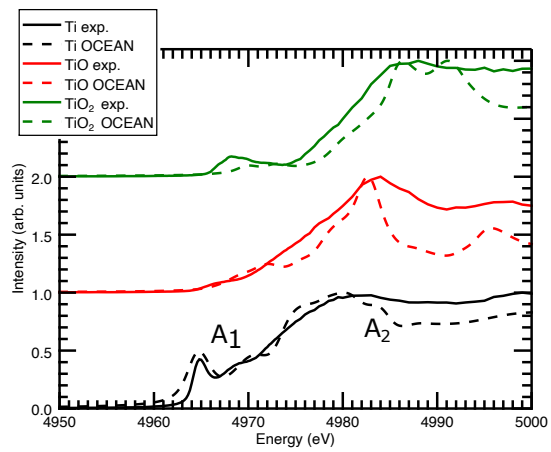

Fig. 2 Comparison between measured (solid lines) and calculated (dashed lines) spectra of K-edge XAS for Ti, TiO, and TiO_2. The spectra are normalized to the respective maximum intensity and offset vertically for clarity.

energies by about 4 eV and 7 eV respectively. This is accurately represented in the OCEAN calculation. Note that the same absolute energy shift was applied to all spectra to match the experimental data.

The feature A_2 is broad in the experimental data and can not be resolved as several features. However, a slight change in the shape of the feature can be seen between the three systems. TiO seems to have the most pronounced shape while Ti has the broadest peak A_2. Despite the efforts of including broadening into the calculation, the peaks in the experimental data remain broader than the calculated results. An additional factor that was not taken into account in this work is vibrational disorder. All calculations have been carried out using a unit cell, which ignores the fact that disorder might introduce an additional broadening to the whole system[64].

Fig. 3 shows a comparison of the extracted pre-edge for all three materials in comparison between experimental data and

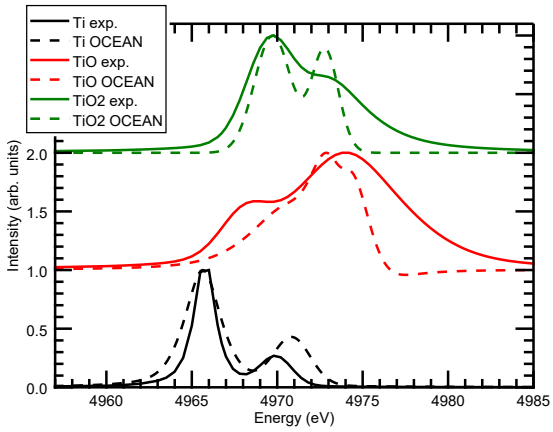

Fig. 3 Comparison between measured (solid lines) and calculated (dashed lines) spectra of the extracted pre-edge. The spectra are normalized to the respective maximum intensity and offset vertically for clarity.

the respective OCEAN calculation. The extraction was done using the previously mentioned fitting of the spectra and separating the pre-edge from the edge step and the excitonic peaks at the edge. The pre-edge region of a metal system can be used to extract information on the coordination number, the oxidation state as well as the spin-state of the absorbing atom[10,65]. Cabaret *et al.*[10] showed that the pre-edge region of TiO_2 can be assigned to both quadrupolar t_{2g} as well as mixed dipolar and quadrupolar e_g transitions. The experimental and theoretical data have a good agreement concerning the pre-edge peak intensities, ratios and positions.

4.3 Titanium L-edge XAS

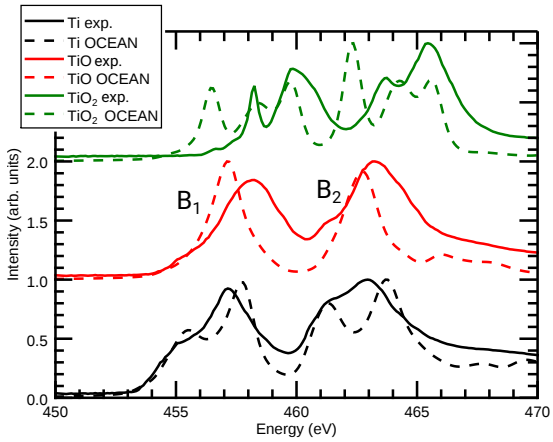

Fig. 4 Comparison between measured (solid lines) and calculated (dashed lines) spectra of L-edge XAS for Ti and TiO. The spectra are normalized to the respective maximum intensity and offset vertically for clarity.

The obtained XAS results at the L edges are shown in Fig. 4 and Fig. 5 as the normalized intensity and as a function of the monochromatic incident photon energy. The previously mentioned t_{2g} molecular orbital is where the three systems differ the most. While at the K edge, this state is only involved in the forbidden quadrupole transition, at the L edge, it is a dipole transition. Thus, the involved transitions have relatively high intensity among the observable transitions. This aspect makes L-edge spectroscopy generally more sensitive for the characterization of titanium oxides. The L edges consist of two main features: B_1 representing the L_{III} and B_2 representing the L_{II} edge transitions[42]. Similar to the K-edge XAS, the spectra shift with higher oxidation state towards higher energies. While the general form of the spectra has a very good agreement in terms of peak form and energy differences between peaks, OCEAN appears to predict the energy chemical shift incorrectly. In OCEAN calculations the frozen core approximation is utilized, assuming that the core-level wavefunction remains constant regardless of the chemical environment[66,67]. Any shift in energy is due to changes in potential energy between systems or sites. While generally accurate, discrepancies in energy alignments may occur when core electrons are directly involved. To resolve this, an all-electron code correction can be utilized, such as the EXCITING code[68]. An analysis calculating a shift ΔE between spectra at the XAS L edge for the three titanium systems validated that the missing chemical shift in the OCEAN calculation can be related to the frozen core approximation.

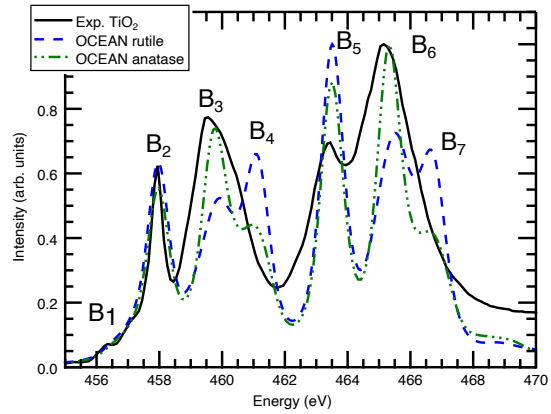

Fig. 5 Comparison between measured TiO_2 sample (solid black line), and calculated (dashed lines) spectra of rutile (blue) and anatase (green) phases at the L-edge. The spectra are normalized to the respective maximum intensity and offset vertically for clarity.

It is worth mentioning that the discrimination capability regarding different chemical species at the L edges is not manifested in the energy shift, but rather in the spectra form and the branching ratio between the L_{III} and L_{II} edges. OCEAN captures the branching ratio between the L_{III} and L_{II} edges correctly, matching the experimentally observed ratio of approximately 1:1. Based on the $2p$ occupation and the available $3d$ states the statistical value of the branching ratio would be 2:1. However, this is not the observation in measured data. Shirley[69] as well as Laskowski *et al.*[70] showed that this is due to mixing between the excitations from $2p_{1/2}$ and $2p_{3/2}$ states which can be observed by setting the exchange term of the BSE Hamiltonian to zero.

4.4 Titanium K-edge XES

An extensive study of the K-edge, in particular Kβ spectroscopy, including OCEAN calculations has been done by Wansleben et al.[34] (Fig. 6). Therefore, we limit our discussion of the K-edge

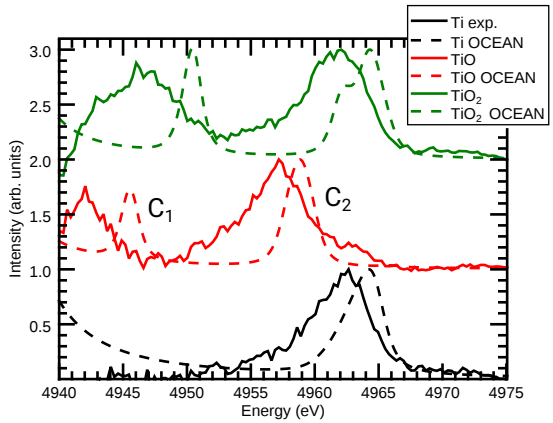

Fig. 6 Comparison between measured spectra (solid lines) from Wansleben *et al.*[34] and calculated (dashed lines) spectra of XES for Ti, TiO, and TiO_2 above the titanium K-edge. The spectra are normalized to the respective maximum intensity and offset vertically for clarity.

	Reference	$K\beta_{2,5} - K\beta_{1,3}$ / eV	$K\beta'' - K\beta_{1,3}$ / eV	$K\beta_{2,5} - K\beta''$ / eV
Ti	exp. - calc.	< 0.1	-	-
	Wansleben et al.	0.3	-	-
TiO	exp. - calc	- 0.4	-3.1	2.2
	Wansleben et al.	- 0.1	-2.4	2.3
TiO_2	exp. - calc.	0.4	-1.9	2.2
	Wansleben et al.	1.1	-1.2	2.3

Table 4 Summarized differences between XES K-edge calculated and measured $K\beta''$ and $K\beta_{2,5}$ peaks relative to the $K\beta_{1,3}$ line and each other in comparison to data taken from Wansleben *et al.*.[34]

XES to the differences between that work and this study. Although the same structure and the same set of parameters were chosen, the calculations were carried out with a different set of pseudopotentials. While Wansleben *et al.* chose pseudopotentials of the Fritz Haber Institute (FHI) from the QUANTUM ESPRESSO website, this work uses pseudopotentials created with the ONCVPSP code, as stated in section 3. Our results and the results from Wansleben *et al.* are presented in Tab. 4. The results are fairly similar with a few exceptions for the $K\beta''$-$K\beta_{1,3}$ differences between the peaks. It is important to note, that the reason for this, next to differences in the calculation, might be due to differences in the fitting and extraction of the spectra.

4.5 Titanium L-edge XES

The results of the comparison of calculated data to experimental data of XES around the L-edges are presented in Fig. 7. Metallic Ti shows two distinct features related to the $L\alpha$ and $L\beta$ transitions[35]. With higher oxidation states transitions from molecular orbitals are important to consider. For the two oxides, the feature D_1 is related to the $e_g \rightarrow 2p_{3/2}$, the feature D_2 to the $t_{2g} \rightarrow 2p_{3/2}$, and D_3 to the $t_{2g} \rightarrow 2p_{1/2}$ transition. The OCEAN spectra show a very good agreement of all three systems regarding peak position, peak number, and energy shifts between the peaks. The occurrence of the peak D_1 for the oxides is correctly predicted as well as the peak ratios between the different systems, which is relevant for the chemical speciation capability.

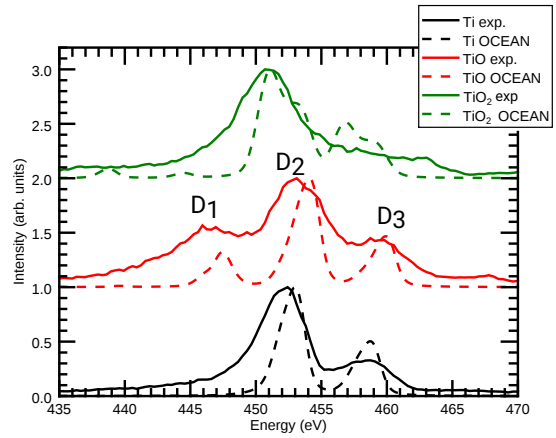

Fig. 7 Comparison between measured (solid lines) and calculated (dashed lines) spectra of XES for Ti, TiO, and TiO_2 above the titanium L-edge. The spectra are normalized to the respective maximum intensity and offset vertically for clarity.

4.6 Oxygen K-edge

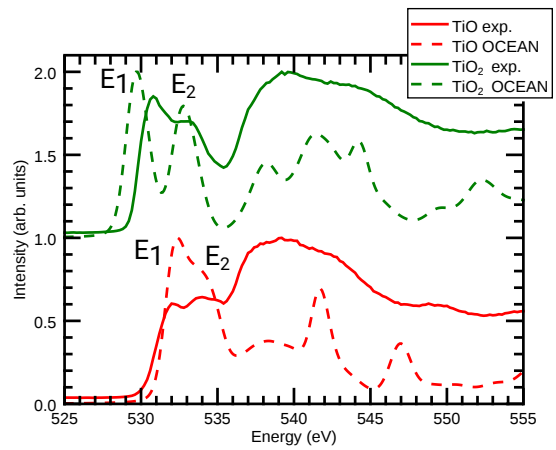

Fig. 8 Comparison between measured (solid lines) and calculated (dashed lines) spectra of O K-edge XAS for TiO, and TiO_2. The spectra are normalized to the respective maximum intensity and offset vertically for clarity.

In addition to titanium K- and L-edge data, the O K edge was analyzed for the titanium oxide systems. The XAS K-edge results are shown in Fig. 8. The analysis shows discrepancies between the calculated O K-edge XAS spectra and the experimental data. These display a significant change around the π^*-resonance with a shift in the energy of 1.2 eV as well as a change regarding the form. As mentioned before, the likely phase of the TiO_2 sample is amorphous, as suggested by the experimental spectrum, which differs from both rutile and anatase. The same is very likely the case for TiO. The splitting of the t_{2g} peak in the oxygen XAS K spectrum of rutile and anatase is a direct result of the distorted octahedra in those two phases. However, the splitting in the experimental spectrum is not that strong, which complicates the calculations of these spectra. This leads to a discrepancy in the relative intensities of the spectra. However, the relative peak positions for each spectrum's π^* resonance from the OCEAN calculation agree with the experiment. The discrepancy in the chemical

shift can be related to the frozen core approximation, similar to the XAS L edge spectra. This was also tested by shifting the spectra with an energy shift calculated from the EXCITING code.

Fig. 9 shows the XES measurement and OCEAN calculation results at the oxygen K edge for TiO and TiO_2. Titanium oxide has a dominant feature that can be associated with the $t_u \longrightarrow 1s$ transition as well as the t_{1u} transition. However, a high-energetic satellite line is observable around 530.6 eV emission photon energy, which has been seen previously in the literature[71] and has been assigned to possible transition metal oxide transitions from the d-band. The titanium dioxide XES reveals an additional low-energy shoulder that can be associated with $t_{1u} \longrightarrow 1s$ transitions. Both are correctly represented in the OCEAN calculations, with a slight overestimation of the chemical shift for TiO_2 which can be associated with the incorrect mixing of O $2p$ and Ti $3d$ states.

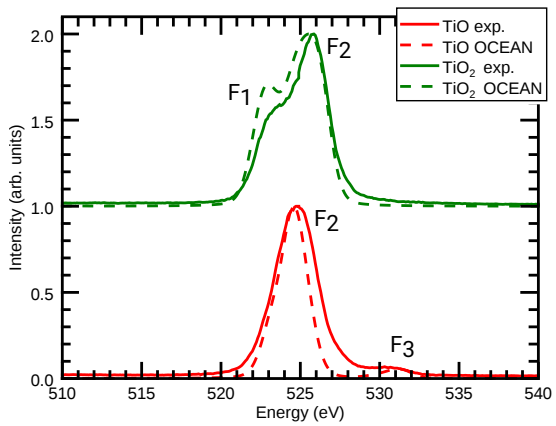

Fig. 9 Comparison between measured (solid lines) and calculated (dashed lines) spectra of O XES for TiO and TiO_2. The spectra are normalized to the respective maximum intensity and offset vertically for clarity.

5 Conclusion

We demonstrate the broad applicability of the OCEAN code by providing an extensive study of titanium and two of its oxides at the K and L edges in absorption and emission spectroscopy. In this study, measurements from different beamlines with the use of different spectrometers were compared. Tab. 3 summarizes the relevant comparisons between peak positions and energy differences between peaks. It presents a good agreement for the systems around the titanium K-edge XAS, including the pre-edge features, the L-edge XES, and the oxygen XES.

While the presented comparison of OCEAN calculations with experimental data demonstrates the broad applicability of the code, it is important to note that there are still discrepancies and limitations. The results at the L-edge XAS as well as the oxygen K-edge show slight discrepancies in the energy alignment, which might be due to the wrong mixing of O $2p$ and Ti $3d$ states. However, the energy shifts at the L-edge provide less information than at the K edge, where the chemical shift indicates the oxidation state of the metal. More important are the relative peak intensities, where the calculation correctly represents the branching ratio of the $L_{II,III}$ edges. Additionally, due to the probable amorphous state of the samples, it was difficult to determine the crystal structure input for the OCEAN calculation of TiO_2. Amorphous samples in the form of thin deposited films are commonly used in XAS experiments due to the interest in technical applications and advantages for measurements. However, the drawback is that it can be difficult to determine the crystal structure input for ab-initio calculations. This trade-off makes it necessary to carefully consider the sample preparation and measurement methods in order to strike a balance between ease of modeling and ease of measurement. In the future, it would be beneficial to conduct thin sample measurements with crystals or evolve the simulation of amorphous samples.

Nevertheless, the use of calibrated instrumentation and the calibration of the energy scales provides a transferable set of data through different sources, energy scales, and measurement techniques and the OCEAN code is able to make broad predictions for all of these measurements based on the same set of input parameters, including the atomic structure and pseudopotentials. Further investigations should focus on solving the limitations of the DFT calculations and including vibrational disorder to the system to reduce the remaining discrepancies.

Conflicts of interest

There are no conflicts to declare.

Acknowledgments

Part of this research was performed within the EMPIR project AEROMET II. This project has received funding from the EMPIR Programme co-financed by the Participating States and from the European Union's Horizon 2020 Research and Innovation Program. Certain commercial materials are identified in this paper in order to specify the experimental procedure adequately. Such identification is not intended to imply recommendation or endorsement by NIST, nor is it intended to imply that the materials or equipment identified are necessarily the best available for the purpose.

Notes and references

1 J. Vinson, J. J. Rehr, J. J. Kas and E. L. Shirley, *Phys. Rev. B 83, 115106*, 2011, 115106.

2 J. Vinson, *Physical Chemistry Chemical Physics*, 2022, **24**, 12787–12803.

3 K. Gilmore, J. Vinson, E. L. Shirley, D. Prendergast, C. D. Pemmaraju, J. J. Kas, F. D. Vila and J. J. Rehr, *Comp. Phys. Comm. 197, 109*, 2015, 109–117.

4 P. Bärmann, L. Haneke, J. M. Wrogemann, M. Winter, O. Guillon, T. Placke and J. Gonzalez-Julian, *ACS Applied Materials & Interfaces*, 2021, **13**, 26074–26083.

5 H. Sibum, V. Güther, O. Roidl, F. Habashi, H. U. Wolf and C. Siemers, *Titanium, Titanium Alloys, and Titanium Compounds*, American Cancer Society, 2017, pp. 1–35.

6 L. Peng, P. Xiong, L. Ma, Y. Yuan, Y. Zhu, D. Chen, X. Luo, J. Lu, K. Amine and G. Yu, *Nature Communications 2017 8:1*, 2017, **8**, 1–10.

7 K. Krishnamoorthy, P. Pazhamalai, S. Sahoo and S.-J. Kim, *Journal of Materials Chemistry A*, 2017, **5**, 5726–5736.

8 H. Kung, *Studies in Surface Science and Catalysis, Amsterdam: Elsevier*, 1989, **45**,.
9 F. Farges, G. E. Brown and J. J. Rehr, *Physical Review B*, 1997, **56**, 1809–1819.
10 D. Cabaret, A. Bordage, A. Juhin, M. Arfaoui and E. Gaudry, *Physical Chemistry Chemical Physics*, 2010, **12**, 5619–5633.
11 V. Mastelaro and E. Zanotto, *Materials*, 2018, **11**, 204.
12 F. M. de Groot, H. Elnaggar, F. Frati, R. p. Wang, M. U. Delgado-Jaime, M. van Veenendaal, J. Fernandez-Rodriguez, M. W. Haverkort, R. J. Green, G. van der Laan, Y. Kvashnin, A. Hariki, H. Ikeno, H. Ramanantoanina, C. Daul, B. Delley, M. Odelius, M. Lundberg, O. Kuhn, S. I. Bokarev, E. Shirley, J. Vinson, K. Gilmore, M. Stener, G. Fronzoni, P. Decleva, P. Kruger, M. Retegan, Y. Joly, C. Vorwerk, C. Draxl, J. Rehr and A. Tanaka, *Journal of Electron Spectroscopy and Related Phenomena*, 2021, **249**, 147061.
13 K. Bzheumikhova, J. Vinson, R. Unterumsberger, Y. Kayser, T. Jach and B. Beckhoff, *Physical Review B*, 2022, **106**, 125133.
14 J. Vinson, T. Jach, W. T. Elam and J. D. Denlinger, *Phys. Rev. B*, 2014, **90**, 205207.
15 A. Andrle, P. Hoenicke, J. Vinson, R. Quintanilha, Q. Saadeh, S. Heidenreich, F. Scholze and V. Soltwisch, *Journal of Applied Crystallography*, 2021, **54**, 402–408.
16 H. Singh, M. Topsakal, K. Attenkofer, T. Wolf, M. Leskes, Y. Duan, F. Wang, J. Vinson, D. Lu and A. I. Frenkel, *Physical Review Materials*, 2018, **2**, 125403.
17 M. Wansleben, J. Vinson, A. Wählisch, K. Bzheumikhova, P. Hönicke, B. Beckhoff and Y. Kayser, *J. Anal. At. Spectrom.*, 2020, **35**, 2679–2685.
18 F. de Groot, *Chemical Reviews*, 2001, **101**, 1779–1808.
19 F. d. Groot, *Coordination Chemistry Reviews*, 2005, **249**, 31–63.
20 F. Reinhardt, B. Beckhoff, H. Eba, B. Kanngiesser, M. Kolbe, M. Mizusawa, M. Müller, B. Pollakowski, K. Sakurai and G. Ulm, *Analytical Chemistry*, 2009, **81**, 1770–1776.
21 G. E. Cutsail and S. Debeer, *ACS Catalysis*, 2022, **12**, 5864–5886.
22 M. Bauer, *Phys. Chem. Chem. Phys.*, 2014, **16**, 13827–13837.
23 J. Kowalska and S. DeBeer, *Biochimica et Biophysica Acta (BBA) - Molecular Cell Research*, 2015, **1853**, 1406–1415.
24 K. Schwalenstocker, J. Paudel, A. W. Kohn, C. Dong, K. M. Van Heuvelen, E. R. Farquhar and F. Li, *Dalton Transactions*, 2016, **45**, 14191–14202.
25 L. Mandić, S. Fazinić and M. Jakšić, *Physical Review A*, 2009, **80**, 042519.
26 B. Beckhoff, *J. Anal. At. Spectrom.*, 2008, **23**, 845–853.
27 B. Beckhoff, A. Gottwald, R. Klein, M. Krumrey, R. Müller, M. Richter, F. Scholze, R. Thornagel and G. Ulm, *Physica Status Solidi (b)*, 2009, **246**, 1415–1434.
28 Müller M, *PhD thesis*, Technische Universität Berlin, Berlin, 2009.
29 R. Klein, M. Krumrey, M. Richter, F. Scholze, R. Thornagel and G. Ulm, *Synchrotron Radiation News*, 2002, **15**, 23–29.
30 B. Beckhoff, R. Klein, M. Krumrey, F. Scholze, R. Thornagel and G. Ulm, *Nuclear Instruments and Methods in Physics Research Section A: Accelerators, Spectrometers, Detectors and Associated Equipment*, 2000, **444**, 480–483.
31 M. Krumrey, *Journal of Synchrotron Radiation*, 1998, **5**, 6–9.
32 M. Krumrey and G. Ulm, *Nucl. Instrum. Methods Phys. Res. A.*, 2001, **467**, 1175–1178.
33 F. Senf, U. Flechsig, F. Eggenstein, W. Gudat, R. Klein, H. Rabus and G. Ulm, *Journal of Synchrotron Radiation*, 1998, **5**, 780–782.
34 M. Wansleben, J. Vinson, I. Holfelder, Y. Kayser and B. Beckhoff, *X-Ray Spectrometry*, 2019, **48**, 102–106.
35 R. Unterumsberger, P. Hönicke, B. Pollakowski-Herrmann, M. Müller and B. Beckhoff, *Spectrochimica Acta Part B: Atomic Spectroscopy*, 2018, **145**, 71–78.
36 M. Krumrey, M. Gerlach, F. Scholze and G. Ulm, *Nucl. Instrum. Methods Phys. Res. A.*, 2006, **568**, 364–368.
37 F. Scholze and M. Procop, *X-Ray Spectrometry*, 2009, **38**, 312–321.
38 R. Thornagel, R. Klein and G. Ulm, *Metrologia*, 2001, **38**, 385–389.
39 L. Anklamm, C. Schlesiger, W. Malzer, D. Grötzsch, M. Neitzel and B. Kanngießer, *Review of Scientific Instruments*, 2014, **85**, 053110.
40 D. Hohlwein, D. Siddons and J. Hastings, *Journal of Applied Crystallography*, 1988, **21**, 911–915.
41 J. Nordgren, G. Bray, S. Cramm, R. Nyholm, J. Rubensson and N. Wassdahl, *Review of Scientific Instruments*, 1989, **60**, 1690–1696.
42 Rainer Unterumsberger, *PhD thesis*, Technische Universität Berlin, Berlin, 2015.
43 D. R. Hamann, *Physical Review B*, 2013, **88**, 085117.
44 S. Glavatskikh and A. I. Gorshkov, *Natural analog of alpha-titanium in the exhalation products of the Great Tolbachik Fissure Eruption (Kamchatka)*, 1992.
45 T.-H. Yu, S.-J. Lin, P. Chao, C.-S. Fang and C.-S. Huang, *Acta Geologica Sinica*, 1974, **2**, 202–2018.
46 R. W. G. Wyckoff, *Acta Crystallographica*, 1965, **18**, 139–139.
47 D. W. Fischer, *Journal of Applied Physics*, 1970, **41**, 3561–3569.
48 K. Tsutsumi, O. Aita and K. Ichikawa, *Physical Review B*, 1977, **15**, 4638–4643.
49 G. S. Henderson, F. M. de Groot and B. J. Moulton, *Reviews in Mineralogy and Geochemistry*, 2014, **78**, 75–138.
50 M. Fracchia, P. Ghigna, A. Minguzzi, A. Vertova, F. Turco, G. Cerrato and D. Meroni, *Nanomaterials*, 2020, **10**, 1224.
51 S. Berardi, J. Kopula Kesavan, L. Amidani, E. M. Meloni, M. Marelli, F. Boscherini, S. Caramori and L. Pasquini, *ACS Applied Materials & Interfaces*, 2020, **12**, 47435–47446.
52 S. O. Kucheyev, T. van Buuren, T. F. Baumann, J. H. Satcher, T. M. Willey, R. W. Meulenberg, T. E. Felter, J. F. Poco, S. A. Gammon and L. J. Terminello, *Physical Review B*, 2004, **69**, 245102.
53 R. Singh, M. Gupta, D. M. Phase and S. K. Mukherjee, *Materi-*

als Research Express, 2019, **6**, 116449.

54 G. Zschornack, *Handbook of X-Ray Data*, Springer Berlin Heidelberg, Berlin, Heidelberg, 2006.

55 H. Enkisch, C. Sternemann, M. Paulus, M. Volmer and W. Schülke, *Physical Review A - Atomic, Molecular, and Optical Physics*, 2004, **70**, 022508.

56 M. Taguchi, T. Uozumi and A. Kotaki, *http://dx.doi.org/10.1143/JPSJ.66.247*, 2013, **66**, 247–256.

57 G. K. Wertheim, M. A. Butler, K. W. West and D. N. E. Buchanan, *Review of Scientific Instruments*, 1974, **45**, 1369–1371.

58 C. Zech, P. Hönicke, Y. Kayser, S. Risse, O. Grätz, M. Stamm and B. Beckhoff, *Journal of Materials Chemistry A*, 2021, **9**, 10231–10239.

59 M. Newville, T. Stensitzki, D. B. Allen and A. Ingargiola, *LMFIT: Non-Linear Least-Square Minimization and Curve-Fitting for Python*, 2014, `https://zenodo.org/record/11813`.

60 M. Newville, *Journal of Physics: Conference Series*, 2013, **430**, 012007.

61 John Vinson, *PhD thesis*, University of Washington, 2012.

62 P. J. W. Weijs, M. T. Czyżyk, J. F. van Acker, W. Speier, J. B. Goedkoop, H. van Leuken, H. J. M. Hendrix, R. A. de Groot, G. van der Laan, K. H. J. Buschow, G. Wiech and J. C. Fuggle, *Physical Review B*, 1990, **41**, 11899–11910.

63 P. I. Sorantin and K. Schwarz, *Inorganic Chemistry*, 1992, **31**, 567–576.

64 J. Vinson, T. Jach, M. Müller, R. Unterumsberger and B. Beckhoff, *Physical Review B*, 2016, **94**, 035163.

65 T. Yamamoto, *X-Ray Spectrometry*, 2008, **37**, 572–584.

66 U. von Barth and C. D. Gelatt, *Physical Review B*, 1980, **21**, 2222–2228.

67 A. Kiejna, G. Kresse, J. Rogal, A. De Sarkar, K. Reuter and M. Scheffler, *Physical Review B*, 2006, **73**, 035404.

68 A. Gulans, S. Kontur, C. Meisenbichler, D. Nabok, P. Pavone, S. Rigamonti, S. Sagmeister, U. Werner and C. Draxl, *Journal of Physics: Condensed Matter*, 2014, **26**, 363202.

69 E. L. Shirley, *Journal of Electron Spectroscopy and Related Phenomena*, 2005, **144-147**, 1187–1190.

70 R. Laskowski and P. Blaha, *Physical Review B*, 2010, **82**, 205104.

71 J. Valjakka, J. Utriainen, T. Berg and J. Tulkki, *Physical Review B*, 1985, **32**, 6892.